Main Manuscript for:

Leveraging Dynamical Symmetries in Two-Dimensional Electronic Spectra to Extract Population Transfer Pathways

Jacob S. Higgins,¹ Anna R. Dardia,¹ Chidera J. Ndife,¹ Lawson T. Lloyd,¹ Elizabeth M. Bain,¹ Gregory S. Engel^{1,*}

This file includes:

Main Text Figures 1 to 6 TOC Graphic

Additional files:

Supporting Information

¹ Department of Chemistry, The Institute for Biophysical Dynamics, The James Franck Institute, The University of Chicago, Chicago, Illinois 60637, United States

^{*} Corresponding author. Email: gsengel@uchicago.edu

Abstract

We present a method to deterministically isolate population transfer kinetics from two-dimensional electronic spectroscopic signals. Central to this analysis is the characterization of how all possible subensembles of excited state systems evolve through the population time. When these dynamics are diagrammatically mapped using double-sided Feynman pathways where population time dynamics are included, a useful symmetry emerges between excited state absorption and ground state bleach recovery dynamics of diagonal and below diagonal cross peak signals. This symmetry allows removal of pathways from the spectra to isolate signals that evolve according to energy transfer kinetics. We describe a regression procedure to fit to energy transfer time constants and characterize the accuracy of the method in a variety of complex excited state systems using simulated two-dimensional spectra. Our results show that the method is robust for extracting ultrafast energy transfer in multistate excitonic systems, systems containing dark states that affect the signal kinetics, and systems with interfering vibrational relaxation pathways. This procedure can be used to accurately extract energy transfer kinetics from a wide variety of condensed phase systems.

I. Introduction

Two-dimensional electronic spectroscopy (2DES) is a technique used extensively over the last two decades to study the excited state behavior of condensed phase systems¹⁻⁴. It has been used to interrogate excited state dynamics in photosynthetic light harvesting complexes⁵⁻¹¹, photobiological systems such as rhodopsin proteins^{12, 13}, synthetic molecular systems¹⁴⁻¹⁷, and materials systems ^{18, 19}. In 2DES, the electronic excitation energies of a system are correlated with the detection energies, revealing how the excited states are coupled^{20, 21}. This coupling can be tracked through the population time with femtosecond precision to monitor the dynamics of processes such as exciton energy transfer (EET). 2DES is a versatile tool to unpack many aspects of excited state system and bath interactions in molecular systems, as one can study spectral lineshapes²²⁻²⁴, coherence dynamics^{3, 4}, and population kinetics^{25, 26} in the signal analysis.

Due to the overlap of multiple peaks and dynamic contributions to 2DES signals, it remains difficult to extract the exact kinetic rates that govern energy transfer^{26, 27}. The illumination of a sample with an ultrafast laser source excites many different dynamical subensembles within the system^{20, 28}. These dynamics can converge onto a single lineshape when the excitation and detection energies of the subensembles are similar, and many of these lineshapes overlap at finite temperatures. The population time evolution at any given point on a 2D spectrum is thus generated from many types of electronic or nuclear motion, such as EET, ground state recovery, coherence, spectral diffusion, and vibrational relaxation²⁹. It has been shown that 2D spectroscopy is capable of resolving the entire energy transfer matrix of spectrally resolved complexes²⁷, and previous reports have extracted population transfer tables in 2D spectra with global fitting analyses⁶ and by using a combination of decay associated and coherence associated spectra³⁰. Another method uses a global fitting procedure based on the variable projection album to fit all spectral components to

a series of complex decaying exponentials to generate decay-associated spectra and coherence-associated spectra³¹.

In this paper, we extend an analysis method to fit to the kinetic parameters for population transfer in two-dimensional spectra. This method has been used to differentiate the kinetics of excitonic pathways in photosynthetic light harvesting systems³², but it can in principle be exported to others. The method differs from other methods in that it accounts for all possible microscopic dynamics of the system and their relative signal contribution and removes signals that interfere with energy transfer kinetics. The paper is outlined as follows. In Section II, we describe the theory of nonlinear spectroscopy and how Feynman pathways allow one to calculate the relative probability that dynamical subensembles contribute to the signal. We then enumerate the types of Feynman pathways in excitonic systems and their relative signal strengths, spectral location, and time evolution. We describe signal processing steps to extract time constant information and methods to improve the accuracy. In Section III, we test the method's accuracy using simulated two-dimensional electronic spectra in a diverse set of systems with increasing complexity, to find that the method is robust to molecular complexes with dark states and interfering resonant vibrations.

II. Theory and Analysis Method

Molecular Response Functions and Their Time Evolution

In 2DES, a nonlinear signal is generated in response to three pulses acting on the system²⁰,

28. The pulses coherently couple the molecular dipoles and generate the third order polarization:

$$P^{3}(t, t_{1}, t_{2}, t_{3}) = \int dt_{1} \int dt_{2} \int dt_{3} E_{3}(t - t_{3}) \cdot$$

$$E_{2}(t - t_{3} - t_{2}) E_{1}(t - t_{3} - t_{2} - t_{1}) R^{3}(t_{1}, t_{2}, t_{3})$$
(1)

This polarization is dependent on three distinct time variables representing the time delay between each pulse, referred to as the coherence time t_1 , the population time (or waiting time) t_2 , and the detection time t_3 . In a semiclassical formalism, the three pulses are treated classically, and the quantum mechanical information of the molecular system is encapsulated in the third order response function R^3 :

$$R^{3}(t_{1},t_{2},t_{3}) = -\left(-\frac{i}{\hbar}\right)^{3} \langle \mu(t_{3}+t_{2}+t_{1}) \left[\mu(t_{2}+t_{1}), \left[\mu(t_{1}), \left[\mu(0), \rho(-\infty)\right]\right]\right] \rangle$$
 (2)

Response functions describe how the ensemble of states reacts to the dipole perturbation induced by the laser pulses³³. The molecular density matrix ρ is acted on by the dipole operator μ^{21} . The nested commutators allow all possible combinations of dipole operators to act on either side of the density matrix, and the brackets $\langle \rangle$ depict an average over the entire thermal ensemble. The magnitude of the transition dipole moment terms $\mu_{ij} = \langle \psi_i | \mu | \psi_j \rangle$ determine the relative probability of transitioning between states i and j^{34} . With multiple dipole interactions acting on the density matrix, permutations from the nested commutators, and averaging over the thermal ensemble, there is a large number of terms in the total third order response function. These terms scale rapidly with the number of dipole-accessible electronic, vibrational, and vibronic states in the system. Each term in the response function describes a particular subensemble, each of which has a probability of contributing to the signal depending on intrinsic properties of the system, such as the transition dipole moments or the transfer rate between the states coupled to the subensemble population.

In this analysis, we use double-sided Feynman pathways to visualize and track the components of the third order response function (Equation 2)^{21,28,35}. Feynman pathways have been used in many physical systems to visualize the behavior of many-body dynamics³⁶. An example Feynman pathway that undergoes population time dynamics is shown in **Figure 1**. The diagonal

lines represent pulses driving transitions on either the bra or ket side of the density matrix. Over each time interval, the signal evolves as either a coherence or a population. For coherences, the signal oscillates with a frequency given by the energy difference between the two states and decays with a dephasing time τ_{deph} :

$$G(t)\alpha e^{i\omega_{ij}t-t/\tau_{deph}} \tag{3}$$

Here, G(t) is the Green function operator that drives time evolution to time t, and $\omega_{ij} = (E_i - E_j)/\hbar^{20,21}$. The coherence generated in the third time interval produces the signal, which we represent with the dashed line. For populations, the signal strength is proportional to the population of the subensemble at time t^{35} . As such, the signal will increase or decrease with the microscopic population dynamics in the system. For example, the pathway shown in **Figure 1** undergoes population dynamics during the population time t_2 , where excitation energy transfers from the excitonic state a to state b with a phenomenological time constant τ_{ab} (shown in the adjacent two excited state system). The signal during t_2 that evolves from this pathway, shown to the right, is directly proportional to the population of exciton b that accumulates due to energy transfer from exciton a. The signal strength is weighted by the transition dipole moments for each laser interaction (in this case $|\mu_a|^2 |\mu_b|^2$, shown as the signal peak).

The population kinetics during the population time t_2 and how the dynamics of all Feynman pathways contribute to the signal are the principle concern of this analysis. We consider each Feynman pathway to represent a particular *dynamical subensemble* of the system, carrying its own population time kinetics due to the system's microscopic behavior. Its relative contribution to the total signal is determined by the dephasing times of the coherences, the kinetics of the populations (typically during t_2), and the transition dipole amplitude from the four light-matter interactions. The 24 possible pathways for a two excited state system with a shared ground state are shown in

Figure S1. These 24 Feynman pathways constitute a basis set that can be used to describe the total response of a larger set of states, including vibrational energy levels. **Table S1** shows each pathway's signal evolution during t_2 and their associated signal strengths.

Time Constant Extraction Method

There are symmetries in the t_2 evolution of diagonal and below diagonal cross peaks of 2D spectra that we can exploit to isolate the time constants for energy transfer. The strongest signals in the diagonal and below diagonal peaks are the ground state bleach (GSB), stimulated emission (SE), and excited state absorption (ESA) signals. For any given diagonal peak a and cross peak a-b, the goal of this analysis is to remove all GSB recovery signals and extraneous ESA signals, thus isolating the dynamics that evolve during the population time due to a-b energy transfer. These signals can be fit exactly to kinetic equations to isolate the phenomenological time constants for energy transfer. The following section describes the Feynman pathways (**Figure 2**), approximations, and steps that this method entails.

Figure 2A-B shows the SE, ESA, GSB, and GSB recovery population and their subsequent population time evolution for a mock exciton e_a diagonal peak and exciton e_a - e_b below diagonal cross peak. For the stimulated emission pathways, the population time dynamics evolve differently between diagonal and below diagonal peaks. The diagonal SE pathway decays with population time due to loss of exciton e_a population as it transfers to exciton e_b , the ground state, or to other states in the system. Assuming monoexponential kinetics for energy transfer and ground state recovery, the exciton e_a loss kinetics for the SE pathways may be modeled as $exp(-t_2/\tau_{ag}) + \sum_{n \neq a} A_n exp(-t_2/\tau_{an})$, where τ_{ag} represents the ground state recovery, and $exp(-t_2/\tau_{an})$ are the system of the second state recovery.

excitons in the system. The cross peak SE pathway increases with population time as e_a - e_b energy transfer occurs but then will decrease as the population subsequently leaves exciton e_b .

At both the e_a diagonal and e_a - e_b cross peak, the ground state bleach and bleach recovery pathways undergo the same time evolution in the population time with a time constant given by the relaxation from exciton a to the ground state. The only difference between the GSB signals of each region is the interaction of the third pulse. The diagonal pathway produces a $|e_a\rangle\langle g|$ coherence while the cross peak pathway produces a $|e_b\rangle\langle g|$ coherence. For clarity, the bleach recovery traces are plotted in Figure 2 with a similar time scale as the energy transfer dynamics. However, recovery to the ground state typically occurs on much slower timescales in most molecular systems (on the order of nanoseconds), meaning they will contribute minimally to short time signals. The presence of features such as conical intersections can speed up the bleach recovery and bring the time constant into the energy transfer regime^{12, 37}, so we include bleach recovery dynamics here to preserve the generalizability of the method. For coherence pathways (Figure 2C), signals associated with coherences will be nearly symmetric about zero (depending on the speed of dephasing and oscillatory frequency) and therefore should not contribute significantly to the retrieved dynamics of the signals. Therefore, the signals should be primarily due to population dynamics.

We consider excited state absorption (ESA) pathways from physical systems in two common limiting cases: weak biexciton coupling and infinite biexciton coupling (**Figure 2A-B**). In ESA pathways, the first two pulses put the system into a singly excited state, and the third pulse drives a transition to a higher excited state. In the case of infinite biexciton coupling, there will be no transition to the higher excited state, so the ESA pathways have no signal strength. In the limiting case of weak biexciton coupling, we assume that the two exciton manifold states are

spanned by direct products of the single exciton states. That is, the biexciton energies are approximately the sum of the single exciton energies.

For a standard ESA pathway on the e_a - e_b cross peak, the first two pulses drive a transition into an e_a population during t_2 , and the third pulse generates the biexciton state f_{ab} . This pathway will evolve over the population time in proportion to the loss of population from exciton a (see Figure 2B, ESA pathway, dashed line; Figure S2). Other ESA pathways on the cross peak include exciton energy transfer (Figure 2B, ESA pathway, solid line). Here, energy will transfer from state a to any state m over the population time, and the third pulse will generate the biexciton state f_{bm} . The signal will thus grow negative amplitude as t_2 increases according to energy transfer kinetics and then decay to zero as the system returns to the ground state. ESA pathways for all m states are possible except for m=b (because the biexciton state f_{bb} is not viable). For generalizability, we include the case m=a to be the standard pathway described at the beginning of this paragraph, whose t₂ signal evolves according to a loss kinetics. Interestingly, there are also energy transfer ESA pathways on the diagonal peaks. On the e_a diagonal (Figure 2A), energy transfers from exciton a at the beginning of the population time to exciton n, and the third pulse generates a biexciton state f_{an} . Similar to the cross peak, the t_2 signal grows negative amplitude as energy transfer occurs and will decay upon ground state recovery. There will be an ESA pathway for each n state with the exception of n=a (for the same reason described above). All of the ESA pathways described here scale with the same transition dipole strength as the corresponding SE and GSB pathways. However, the amplitudes of the signals are likely weaker due to lifetime broadening of the shorter-lived biexciton coherence over t3. The shorter dephasing time spreads the signal over a broader area on the detection axis, which reduces the contribution to each point³³, ³⁸. The relative weakness of ESA signals can be seen in the largely positive diagonal and belowdiagonal 2DES signals of photosynthetic light harvesting complexes^{6, 8, 25, 39, 40}, demonstrating that the positive SE and GSB pathways produce stronger signals in these regions.

For every set of ESA pathways on a diagonal peak a and below diagonal cross peak a-b, all pathways not corresponding to the t2 evolution of stimulated emission pathways will evolve with the same kinetics on the diagonal and cross peak. This is illustrated in an example three exciton system in Figure S2A-B. The exciton 3 diagonal has two ESA pathways (downhill energy transfer to excitons 1 and 2), and the exciton 3-1 cross peak has two ESA pathways (loss of exciton 3 and downhill energy transfer to exciton 2). Between these two peaks, the exciton 3-2 energy transfer pathways evolve according to the same kinetics. We consider these pathways to be extraneous for the 3-1 cross peak because they do not correspond to exciton 3-1 energy transfer. In contrast, the remaining pathways evolve differently between the diagonal and cross peak. The 3-1 energy transfer pathway on the diagonal evolves with the same kinetics as the SE pathway on the cross peak (but with a negative sign, see Figure S2D). Similarly, the exciton 3 cross peak pathway evolves according to the diagonal SE pathway (but again, with a negative sign, see Figure **S2C**). This example can be inductively generalized to any n exciton system. The symmetry between the extraneous pathways and the asymmetry between relevant energy transfer pathways allow us to remove extraneous ESA pathways unrelated to energy transfer between the two excitons.

We take advantage of these symmetries in the bleach recovery and ESA pathways to remove their contribution to the signal evolution. At each peak, the pathways scale with the same transition dipole strength, but the strength is different between peaks. We correct for this difference by first normalizing each signal:

$$\operatorname{norm}(\operatorname{Sig}(T)) = \frac{\operatorname{Sig}(T) - \operatorname{Sig}(T_i)}{|\operatorname{Sig}(T_f) - \operatorname{Sig}(T_i)|} \tag{4}$$

Here, T_i and T_f are the initial and final t_2 values for each time interval. The normalization step removes the amplitude differences between the diagonal and cross peaks but keeps the difference curvature due population transfer rates. We subtract the normalized diagonal signal from its corresponding normalized lower diagonal cross peak signal to remove the bleach recovery contribution, maintain the stimulated emission kinetics, and keep only the ESA pathways that correspond to SE kinetics (**Figure S2**). Because the relevant ESA traces evolve equally and oppositely to the SE kinetics on the corresponding peak, the subtraction step will be additive for these kinetics. The time constant for the subtracted signal is a parameter that can be used to fit to energy transfer time constants.

The schematic of steps for isolating the kinetic rate constants is shown in **Figure 3**. For clarity, we use sequential exciton numbering, where exciton 1 is the lowest energy. First, diagonal and cross peak regions of the excitonic peaks are averaged using circular windows. Averaging over finite regions removes the bath dynamics from the signal such as vibrational relaxation and spectral diffusion (see **Figure S5**). These dynamics affect the lineshape evolution in the spectra, and averaging removes this effect so that the signal evolves in time exclusively from excitonic dynamics. Then, a population time interval is selected for curve fitting, typically from times between 50 and 100 fs to about half the experimental time, typically \sim 1000 fs. The fitting procedure is then performed starting with energy transfer between the lowest two excitonic states. The 2 diagonal and 2-1 cross peak are normalized according to Equation 4 and then subtracted from one another. If necessary, the τ_{IL} time constant can be obtained from the exciton 1 diagonal. The bleach recovery signal is removed in the subtraction. The stimulated emission signals and remaining ESA signals evolve according to 2-1 energy transfer. Thus, the fit time constant for the subtracted signal must be the energy transfer time constant τ_{IL} .

The procedure then moves to the next highest excitonic state. The time constant τ_{3L} ('3 loss,' or transfer from exciton 3 to other states) is estimated as the short time constant in a biexponential fit to the 3 diagonal. This τ_{3L} value must satisfy the other energy transfer time constants τ_{32} and τ_{31} according to $k_{3L}=\frac{1}{\tau_{3L}}=\frac{1}{\tau_{31}}+\frac{1}{\tau_{32}}$. The 3 diagonal and below diagonal cross peaks are then normalized, and one cross peak is selected to be subtracted from the diagonal. Typically, the 3-1 cross peak is chosen to ensure a good fit to the subtracted time constant because the peak signal monotonically increases over short experimental times, rather than the 3-2 cross peak, which often has flatter curvature due to energy transfer in and out of exciton 2. The normalized diagonal and cross peak signals are subtracted from one another, and the remaining signal is fit to a set of kinetic parameters. These parameters are typically a monoexponential decay function in excitonic signals, though other functions can be used if they better fit the data. The subtracted fit is used as an empirical constraint for the numerical procedure. Solutions to differential equations for energy transfer are numerically calculated to fit to the diagonal and cross peak stimulated emission signals, which are also normalized, subtracted, and fit to the same kinetic parameters. The resulting time constant value is compared to the experimental data. The calculation is repeated for all short time values of τ_{31} and τ_{32} under the constraint of τ_{3L} , and the combination that best matches the experimental subtracted time constant is selected as the best fit for energy transfer. (Note: τ_{21} has already been calculated, as it is used as a parameter in the differential equation.) The numerical fitting procedure is done for higher energy levels as necessary.

This entire analysis, starting from the normalization of the 2 diagonal and 2-1 cross peak, is then repeated with different time intervals until the time interval spans the entire experimental time, typically ~2000 fs. For each time interval, the goodness of fit for the numerical signals is

evaluated by calculating the root-mean-squared difference between the experimental subtracted 2D signals and the numerically calculated subtracted signals. There is a range of best-fitting time intervals are averaged over to produce the final time constant values for EET. This final averaging step minimizes error due to the arbitrary choice of time interval. In the **Supporting Information**, we discuss how this method can be extended to other systems.

We demonstrate this process with data from the Fenna-Matthews-Olson (FMO) complex from green sulfur bacteria in reducing conditions. This analysis has been conducted in a previous study without the final population time interval average³². Figure 4A shows a two-dimensional spectrum of FMO at population time 800 fs. The three diagonal peaks represent excitons 4, 2, and 1, which constitute a major energy transfer pathway through the complex²⁵. The time traces are averaged using a 70 cm⁻¹ circular window. Figure 4B-E depicts the signal subtraction process using a population time window range from 100 to 2000 fs. Figure 4B is the monoexponential fit to the normalized 2 diagonal subtracted from the normalized 2-1 cross peak, which isolates the τ_{21} time constant. Figure 4C is the fit to the averaged exciton 4 diagonal peak, where the short time constant τ_l =225 fs is estimated as the exciton 4 loss time constant. The monoexponential fit to the normalized 4 diagonal subtracted from the normalized 4-1 cross peak (Figure 4D) is then reproduced in the numerical simulation (**Figure 4E**) such that τ_{41} and τ_{42} satisfy the τ_{4L} constraint. After repeating this process over population time end points from 600 to 2000 fs, we find that the lowest root-mean-square error falls in the range from 1700 to 2000 fs (**Figure 4F**). After averaging over this range, we obtain the final averaged time constants \(\tau_{2/ave}=453\) fs, \(\tau_{42ave}=409\) fs, and τ_{41ave} =496 fs.

III. Results

Global Response and Method Accuracy for Excitonic Systems

We simulated two-dimensional spectra of multi state systems by calculating each component of the total response in the time domain, following the procedure laid out in Ref. ²⁸. All combinations of Feynman pathways from a system with two excited states (Figure S1) were used to form a basis set to model systems with multiple excited states, taking care not to double count pathways. We then Fourier transformed the t_1 and t_3 axes of the total response to obtain ω_1 and ω . Unless stated otherwise, the spectra were simulated near the limit of infinite biexciton coupling. Three classes of energy transfer systems were simulated, shown in Figure 5, to understand the accuracy of this method under differing excited state structures. The first system (Figure 5A) is a standard excitonic model, featuring downhill energy transfer between three electronic excited states. All states are dipole allowed from the ground state and have a ground state recovery time τ_g that is at least an order of magnitude higher than the energy transfer times. The second system (Figure 5B) is the dark state system, where a fourth electronic state is added with no transition dipole moment between the state and the ground state. Excitons are allowed to transfer between this state and the three bright excited electronic states, however, so its presence will affect the EET kinetics of the three bright excitons. In this analysis, we include systems with a dark state between excitons 1 and 2 and between excitons 2 and 3 and show that the dark state only affects the extracted kinetics of adjacent excitons. In the third system (Figure 5C), a vibrational energy level is added to each excited state whose energy gap is resonant with the adjacent exciton energy gap. In this system, vibrational relaxation within one exciton will create below diagonal cross peak signals that constructively interfere with EET signals (see Figure S5). We discuss the effect that each of these additions has on the population time traces in the

Supporting Information. We will show that while dark state kinetics and vibrational relaxation affect the cross peak signal growth, the analysis method still accurately extracts the kinetic parameters for exciton energy transfer.

We test the method's accuracy in the two limiting ESA cases and the assumption that coherence pathways don't impact the method. We characterize the accuracy of the standard system parameters when the relative contribution the signal strength of excited state absorption and coherence pathways is increased (Figure 6). The former is done by increasing the dipole ratio μ_{fe}/μ_{eg} , where μ_{eg} is the dipole moment of the ground to excited state transition, and μ_{fe} is the dipole moment from the first excited state to the biexciton state. Figure 6A shows the error in the standard three exciton system as the μ_{fe}/μ_{eg} dipole ratio ranges from zero to one. In most cases, the error falls below 15%, demonstrating that the method works between the two limiting cases of infinite and weak biexciton coupling. For coherence pathways, dephasing times in the hundreds of femtoseconds range (which are typical dephasing times for vibrational and vibronic coherences⁴¹-⁴³) might interfere with the exponential pathways involving energy transfer. The presence of longlived coherent signals observed in multiple photosynthetic systems^{5, 41, 44-46} might affect the time constant extraction. Figure 6B shows the error as the dephasing time for excited state coherences is increased from below 100 fs to 500 fs. The dephasing time has little effect on the accuracy for any of the three EET time constants. The coherence pathways modulate the signal in the population time, but they do little to affect the monotonic signal kinetics and therefore the exponential fits. This result will hold true for both excited state electronic or vibronic coherences and ground state vibrational coherences.

We now compare the method's accuracy for the systems shown in **Figure 5** using multiple kinetic schemes for energy transfer. **Tables S7-10** show the percent errors for each time constant

for the standard system, two dark state systems, and the vibrational system. For the standard system (**Table S7**), we find that the method is accurate for energy transfer systems with subpicosecond kinetics, as all but one time constant is fit to within 15% accuracy. The τ_{31} time constants are all fit within 10% accuracy, and the τ_{21} constants are all extracted within 5% accuracy. In schemes with picosecond energy transfer constants, the method tends to inaccurately calculate the slow time constant with errors above 20%. However, the accuracy of the subpicosecond time constants remains within 15% (**Table S7**). This effect is likely due to the regression more accurately fitting signals that evolve several e-folds through the population time (as experimental timeframes typically range from 0 to 2000 fs). We should note that for the standard system, averaging over multiple time intervals does not significantly improve the accuracy of the method.

We find that dark states only affect the accuracy of the time constants for adjacent excitons that are directly involved in energy transfer with the dark states. **Table S8** shows the method accuracy for multiple kinetic schemes when a dark state is added between excitons 1 and 2. For each scheme, the energy transfer to (τ_{2d}) and from (τ_{dl}) the dark state is changed to test how the dark state kinetics affect the method's accuracy. All τ_{2l} errors are greater than 15%. This error is due to the kinetic sink effect between excitons 2 and 1. However, τ_{3l} and τ_{32} remain accurate for all schemes where energy is allowed to flow to and from the dark state, with many of the errors falling below 5%. This result is notable because the presence of dark states on lower exciton manifolds does not disrupt the accuracy of the calculation for higher excitonic states despite the fact that the fit to τ_{3l} and τ_{32} relies on knowledge of τ_{2l} (see Section II). **Table S9** shows the method accuracy when a dark state is added between excitons 2 and 3. In this model, τ_{2l} remains accurate for all kinetic schemes within 5%. However, τ_{32} and τ_{3l} are each off by >30% for every scheme for the same kinetic sinking effect described above. In the method, τ_{3l} and τ_{32} are simultaneously

calculated to reproduce the time constant of the subtracted signal (see **Figure 3**, step 7). An error in one time constant due to the kinetic trap would therefore introduce an error in the other time constant. For both dark state systems, averaging over multiple time intervals does not improve the method accuracy. We should note that the method is only accurate when excitons are allowed to flow in and out of the dark state. **Tables S8-9** show the method is highly inaccurate for all time constants when energy does not flow back. Thus, in systems containing dark states that couple to the excitonic states, knowledge of the electronic states and their couplings must be known *a priori* to know which calculated time constants will be accurate.

In the final step of the analysis, multiple time intervals are averaged to minimize errors due to arbitrary choice of population time intervals (Figure 3, step 8). This step does not improve the accuracy of the standard and dark state systems, but it markedly improves the accuracy of the vibrational system. Table S10 shows the method accuracy for multiple kinetic schemes when the slow relaxation of resonant vibrations interferes with below diagonal energy transfer cross peaks (see Figure S6), as described in the previous section. The analysis method remains accurate to 10% for all time constants after averaging over multiple population time intervals. For the vibrationsl system, we find that the fits with the smallest least squares fit to the subtracted signal and those which most accurately extract the energy transfer time constants occur when shorter time intervals are averaged (e.g. from 50-1050 fs to 50-1775 fs). This range is long enough to capture multiple energy transfer e-folds but short enough to minimize the effect of picosecond signal changes due to vibrational relaxation. This result is in contrast to the purely electronic standard and dark state kinetic systems, where the smallest least squares error and most accurate time constant fits occur over larger time intervals. In experimental molecular spectra, there will be slow signals due to vibrational relaxation and other nuclear motion not completely removed from the signal averaging^{47, 48}. It is necessary to average over the time intervals to most accurately extract the kinetic time constants. The need to average over shorter time intervals could therefore show the presence of interfering Stokes shift signals in experimental 2D measurements.

For all system types, the error in the time constant τ_{2l} is smaller than τ_{2l} and τ_{2l} . (**Tables S7-10**). This result is due to a combination of two effects. The first is the relatively smaller number of kinetic pathways involving 2-1 energy transfer. For the 2 diagonal and 2-1 cross peak, there are no competing kinetic pathways that influence the signal. Conversely, exciton migration through both the exciton 3-2-1 pathway and the direct 3-1 pathway both cause the 3 diagonal to decrease and the 3-1 cross peak to increase with time. The competing pathways amplify small errors in the analysis because the τ_{3l} and τ_{32} time constants because both τ_{3l} and τ_{32} are fit simultaneously, as described above. The second effect is the approximation of the exciton 3 loss pathway (**Figure 3**, step 4). The τ_{3l} time constant is estimated as the short time constant of the diagonal. The loss rate constrains τ_{32} and τ_{3l} because the sum $k_{32} + k_{3l}$ must equal k_{3l} , but other Feynman pathways such as the ESA pathways and the ground state bleach recovery contribute to signal loss on the 3 diagonal. This approximation thus limits the possibility of reproducing the subtracted signal with complete accuracy. However, we have shown that the time constants are still fit within 15% accuracy despite these limitations.

IV. Conclusion

We develop and characterize a method to accurately fit two-dimensional spectra to elementary kinetic rates for multistate energy transfer systems. We simulated two-dimensional spectra for standard multiexcitonic systems undergoing energy transfer, systems comprised of dark states that act as kinetic traps for energy transfer, and systems with resonant vibrations that undergo

vibrational relaxation. The method remains accurate in the efficient energy transfer regime in two common limiting cases for excited state absorption pathways — weak and infinite biexciton coupling — and when the signals are convoluted by long-lived coherence and interfering vibrational relaxation pathways. When dark states are present the system, the fitting is accurate for energy transfer between states that are not adjacent to the dark state. Extracting accurate kinetic information from EET systems can provide information on the subtle microscopic parameters that influence and system and allow for precise comparative analyses between systems with slight differences, such as point mutations and functional group substitutions. As such, the method is widely applicable to excitonic systems undergoing downhill population transfer.

Supporting Information

Global response simulation details; cancellation of excited stat absorption signals; nuclear signal evolution; accuracy checks and sensitivity analysis; simulated spectra time constants; method accuracy data; and extension of analysis method.

Acknowledgements

This research was supported by the Department of Defense under the Vannevar Bush Fellowship (N00014-16-1-2513), the Air Force Office of Scientific Research (FA9550-18-1-0099), and the NSF QuBBE Quantum Leap Challenge Institute (NSF OMA-2121044). NSF (grant no. CHE-1900359) partially supported C.J.N., E.M.B, and A.R.D. The DOE Office of Science (award no. DE-SC0020131) partially supported J.S.H. Support was also provided by the Chicago MRSEC, funded by the NSF through grant DMR-1420709. J.S.H. and E.M.B. were supported individually in part by NSF-GRFP fellowships.

References

- 1. Cho, M.; Vaswani, H. M.; Brixner, T.; Stenger, J.; Fleming, G. R., Exciton Analysis in 2D Electronic Spectroscopy. *The Journal of Physical Chemistry B* **2005**, *109* (21), 10542-10556.
- 2. Jeon, J. P., S; Cho, M, Two-dimensional Optical Spectroscopy: Theory and Experiment. In *Encyclopedia of Analytical Chemistry*, John Wiley & Sons 2010.
- 3. Scholes, G. D.; Fleming, G. R.; Chen, L. X.; Aspuru-Guzik, A.; Buchleitner, A.; Coker, D. F.; Engel, G. S.; van Grondelle, R.; Ishizaki, A.; Jonas, D. M.; Lundeen, J. S.; McCusker, J. K.; Mukamel, S.; Ogilvie, J. P.; Olaya-Castro, A.; Ratner, M. A.; Spano, F. C.; Whaley, K. B.; Zhu, X., Using coherence to enhance function in chemical and biophysical systems. *Nature* **2017**, *543* (7647), 647-656.
- 4. Wang, L.; Allodi, M. A.; Engel, G. S., Quantum coherences reveal excited-state dynamics in biophysical systems. *Nature Reviews Chemistry* **2019**, *3* (8), 477-490.
- 5. Panitchayangkoon, G.; Hayes, D.; Fransted, K. A.; Caram, J. R.; Harel, E.; Wen, J.; Blankenship, R. E.; Engel, G. S., Long-lived quantum coherence in photosynthetic complexes at physiological temperature. *Proceedings of the National Academy of Sciences* **2010**, *107* (29), 12766-12770.
- 6. Dostál, J.; Pšenčík, J.; Zigmantas, D., In situ mapping of the energy flow through the entire photosynthetic apparatus. *Nature Chemistry* **2016**, *8*, 705.
- 7. Duan, H.-G.; Prokhorenko, V. I.; Cogdell, R. J.; Ashraf, K.; Stevens, A. L.; Thorwart, M.; Miller, R. J. D., Nature does not rely on long-lived electronic quantum coherence for photosynthetic energy transfer. *Proceedings of the National Academy of Sciences* **2017**, *114* (32), 8493-8498.
- 8. Fuller, F. D.; Pan, J.; Gelzinis, A.; Butkus, V.; Senlik, S. S.; Wilcox, D. E.; Yocum, C. F.; Valkunas, L.; Abramavicius, D.; Ogilvie, J. P., Vibronic coherence in oxygenic photosynthesis. *Nature Chemistry* **2014**, *6* (8), 706-711.
- 9. Son, M.; Pinnola, A.; Bassi, R.; Schlau-Cohen, G. S., The Electronic Structure of Lutein 2 Is Optimized for Light Harvesting in Plants. *Chem* **2019**, *5* (3), 575-584.
- 10. Son, M.; Pinnola, A.; Gordon, S. C.; Bassi, R.; Schlau-Cohen, G. S., Observation of dissipative chlorophyll-to-carotenoid energy transfer in light-harvesting complex II in membrane nanodiscs. *Nature Communications* **2020**, *11* (1), 1295.
- 11. Brixner, T.; Stenger, J.; Vaswani, H. M.; Cho, M.; Blankenship, R. E.; Fleming, G. R., Two-dimensional spectroscopy of electronic couplings in photosynthesis. *Nature* **2005**, *434* (7033), 625-628.
- 12. Johnson, P. J. M.; Farag, M. H.; Halpin, A.; Morizumi, T.; Prokhorenko, V. I.; Knoester, J.; Jansen, T. L. C.; Ernst, O. P.; Miller, R. J. D., The Primary Photochemistry of Vision Occurs at the Molecular Speed Limit. *The Journal of Physical Chemistry B* **2017**, *121* (16), 4040-4047.
- 13. Gozem, S.; Johnson, P. J. M.; Halpin, A.; Luk, H. L.; Morizumi, T.; Prokhorenko, V. I.; Ernst, O. P.; Olivucci, M.; Miller, R. J. D., Excited-State Vibronic Dynamics of Bacteriorhodopsin from Two-Dimensional Electronic Photon Echo Spectroscopy and Multiconfigurational Quantum Chemistry. *The Journal of Physical Chemistry Letters* **2020**, *11* (10), 3889-3896.

- 14. Wang, L.; Griffin, G. B.; Zhang, A.; Zhai, F.; Williams, N. E.; Jordan, R. F.; Engel, G. S., Controlling quantum-beating signals in 2D electronic spectra by packing synthetic heterodimers on single-walled carbon nanotubes. *Nature Chemistry* **2017**, *9* (3), 219-225.
- 15. Sohail, S. H.; Otto, J. P.; Cunningham, P. D.; Kim, Y. C.; Wood, R. E.; Allodi, M. A.; Higgins, J. S.; Melinger, J. S.; Engel, G. S., DNA scaffold supports long-lived vibronic coherence in an indodicarbocyanine (Cy5) dimer. *Chemical Science* **2020**, *11* (32), 8546-8557.
- 16. Milota, F.; Prokhorenko, V. I.; Mancal, T.; von Berlepsch, H.; Bixner, O.; Kauffmann, H. F.; Hauer, J., Vibronic and Vibrational Coherences in Two-Dimensional Electronic Spectra of Supramolecular J-Aggregates. *The Journal of Physical Chemistry A* **2013**, *117* (29), 6007-6014.
- 17. Lim, J.; Paleček, D.; Caycedo-Soler, F.; Lincoln, C. N.; Prior, J.; von Berlepsch, H.; Huelga, S. F.; Plenio, M. B.; Zigmantas, D.; Hauer, J., Vibronic origin of long-lived coherence in an artificial molecular light harvester. *Nature Communications* **2015**, *6* (1), 7755.
- 18. Wood, R. E.; Lloyd, L. T.; Mujid, F.; Wang, L.; Allodi, M. A.; Gao, H.; Mazuski, R.; Ting, P. C.; Xie, S.; Park, J.; Engel, G. S., Evidence for the Dominance of Carrier-Induced Band Gap Renormalization over Biexciton Formation in Cryogenic Ultrafast Experiments on MoS₂ Monolayers. *J Phys Chem Lett* **2020**, *11* (7), 2658-2666.
- 19. Smallwood, C. L.; Cundiff, S. T., Multidimensional Coherent Spectroscopy of Semiconductors. *Laser & Photonics Reviews* **2018**, *12* (12), 1800171.
- 20. Mukamel, S., *Principles of Nonlinear Optical Spectroscopy*. Oxford University Press: New York, 1995.
- 21. Tokmakoff, A., Time-Dependent Quantum Mechanics and Spectroscopy. 2014; p tdqms.uchicago.edu.
- 22. Roberts, S. T.; Loparo, J. J.; Tokmakoff, A., Characterization of spectral diffusion from two-dimensional line shapes. *The Journal of Chemical Physics* **2006**, *125* (8), 084502.
- 23. Kwak, K.; Park, S.; Finkelstein, I. J.; Fayer, M. D., Frequency-frequency correlation functions and apodization in two-dimensional infrared vibrational echo spectroscopy: A new approach. *The Journal of Chemical Physics* **2007**, *127* (12), 124503.
- 24. Fenn, E. E.; Fayer, M. D., Extracting 2D IR frequency-frequency correlation functions from two component systems. *The Journal of Chemical Physics* **2011**, *135* (7), 074502.
- 25. Allodi, M. A.; Otto, J. P.; Sohail, S. H.; Saer, R. G.; Wood, R. E.; Rolczynski, B. S.; Massey, S. C.; Ting, P.-C.; Blankenship, R. E.; Engel, G. S., Redox Conditions Affect Ultrafast Exciton Transport in Photosynthetic Pigment–Protein Complexes. *The Journal of Physical Chemistry Letters* **2018**, *9* (1), 89-95.
- 26. Thyrhaug, E.; Žídek, K.; Dostál, J.; Bína, D.; Zigmantas, D., Exciton Structure and Energy Transfer in the Fenna–Matthews–Olson Complex. *The Journal of Physical Chemistry Letters* **2016**, *7* (9), 1653-1660.
- 27. Dostál, J.; Benešová, B.; Brixner, T., Two-dimensional electronic spectroscopy can fully characterize the population transfer in molecular systems. *The Journal of Chemical Physics* **2016**, *145* (12), 124312.
- 28. Hamm, P. Z., Martin, *Concepts and Methods of 2D Infrared Spectroscopy*. Cambridge University Press: 2011.
- 29. Silbey, R., Description of quantum effects in the condensed phase. *Procedia Chemistry* **2011,** *3* (1), 188-197.
- 30. Gururangan, K.; Harel, E., Coherent and dissipative quantum process tensor reconstructions in two-dimensional electronic spectroscopy. *The Journal of Chemical Physics* **2019**, *150* (16), 164127.

- 31. Volpato, A.; Bolzonello, L.; Meneghin, E.; Collini, E., Global analysis of coherence and population dynamics in 2D electronic spectroscopy. *Opt. Express* **2016**, *24* (21), 24773-24785.
- 32. Higgins, J. S.; Lloyd, L. T.; Sohail, S. H.; Allodi, M. A.; Otto, J. P.; Saer, R. G.; Wood, R. E.; Massey, S. C.; Ting, P.-C.; Blankenship, R. E.; Engel, G. S., Photosynthesis tunes quantum mechanical mixing of electronic and vibrational states to steer exciton energy transfer. *Proceedings of the National Academy of Sciences* **2021**.
- 33. Boyd, R., Nonlinear Optics. 3rd ed.; Academic Press: 2008.
- 34. Cohen-Tannoudji, C. D., Bernard; Laloe, Frank, *Quantum Mechanics*. 1 ed.; Wiley, 1991.
- 35. Yang, M.; Fleming, G. R., Third-order nonlinear optical response of energy transfer systems. *The Journal of Chemical Physics* **1999**, *111* (1), 27-39.
- 36. Mattuck, R. D., *A Guide to Feynman Diagrams in the Many-Body Problem*. 2nd ed.; Dover Publications: 1992.
- 37. Polli, D.; Altoè, P.; Weingart, O.; Spillane, K. M.; Manzoni, C.; Brida, D.; Tomasello, G.; Orlandi, G.; Kukura, P.; Mathies, R. A.; Garavelli, M.; Cerullo, G., Conical intersection dynamics of the primary photoisomerization event in vision. *Nature* **2010**, *467* (7314), 440-443.
- 38. Harris, D. C. B., Michael D., *Symmetry and Spectroscopy: An Introduction to Vibrational and Electronic Spectroscopy.* Oxford University Press, Inc.: New York, 1978.
- 39. Sohail, S. H.; Dahlberg, P. D.; Allodi, M. A.; Massey, S. C.; Ting, P.-C.; Martin, E. C.; Hunter, C. N.; Engel, G. S., Communication: Broad manifold of excitonic states in light-harvesting complex 1 promotes efficient unidirectional energy transfer in vivo. *The Journal of*

Chemical Physics 2017, 147 (13), 131101.

- 40. Dahlberg, P. D.; Ting, P.-C.; Massey, S. C.; Allodi, M. A.; Martin, E. C.; Hunter, C. N.; Engel, G. S., Mapping the ultrafast flow of harvested solar energy in living photosynthetic cells. *Nature Communications* **2017**, *8* (1), 988.
- 41. Higgins, J. S.; Hollingsworth, W. R.; Lloyd, L. T.; Engel, G. S., Quantum Coherence in Chemical and Photobiological Systems. In *Emerging Trends in Chemical Applications of Lasers*, American Chemical Society: 2021; Vol. 1398, pp 411-436.
- 42. Christensson, N.; Kauffmann, H. F.; Pullerits, T.; Mančal, T., Origin of Long-Lived Coherences in Light-Harvesting Complexes. *Journal of Physical Chemistry B* **2012**, *116* (25), 7449-7454.
- 43. Yeh, S.-H.; Hoehn, R. D.; Allodi, M. A.; Engel, G. S.; Kais, S., Elucidation of near-resonance vibronic coherence lifetimes by nonadiabatic electronic-vibrational state character mixing. *Proceedings of the National Academy of Sciences* **2019**, *116* (37), 18263.
- 44. Engel, G. S.; Calhoun, T. R.; Read, E. L.; Ahn, T.-K.; Mančal, T.; Cheng, Y.-C.; Blankenship, R. E.; Fleming, G. R., Evidence for wavelike energy transfer through quantum coherence in photosynthetic systems. *Nature* **2007**, *446* (7137), 782-786.
- 45. Maiuri, M.; Ostroumov, E. E.; Saer, R. G.; Blankenship, R. E.; Scholes, G. D., Coherent wavepackets in the Fenna–Matthews–Olson complex are robust to excitonic-structure perturbations caused by mutagenesis. *Nature Chemistry* **2018**, *10*, 177.
- 46. Higgins, J. S.; Allodi, M. A.; Lloyd, L. T.; Otto, J. P.; Sohail, S. H.; Saer, R. G.; Wood, R. E.; Massey, S. C.; Ting, P.-C.; Blankenship, R. E.; Engel, G. S., Redox conditions correlated with vibronic coupling modulate quantum beats in photosynthetic pigment–protein complexes. *Proceedings of the National Academy of Sciences* **2021**, *118* (49), e2112817118.

- 47. Mirkovic, T.; Ostroumov, E. E.; Anna, J. M.; van Grondelle, R.; Govindjee; Scholes, G. D., Light Absorption and Energy Transfer in the Antenna Complexes of Photosynthetic Organisms. *Chemical Reviews* **2017**, *117* (2), 249-293.
- 48. Novoderezhkin, V. I.; van Grondelle, R., Physical origins and models of energy transfer in photosynthetic light-harvesting. *Physical Chemistry Chemical Physics* **2010**, *12* (27), 7352-7365.

Figures

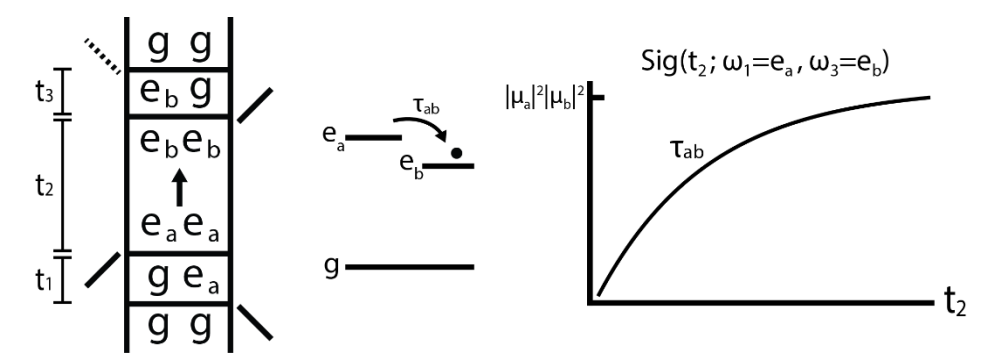


Figure 1. Double-sided Feynman pathway representing a dynamical subensemble that undergoes population transfer from state e_a to e_b during the population time, t_2 . The excitation and detection axes ω_l and ω_3 are respectively given by the bra-ket energy difference during t_1 and t_3 . The signal evolution through t_2 is proportional to the population of excitation probed from e_b that began in e_a at t_2 =0. As such, the pathway will evolve with the kinetics of energy transfer such that its rise time will be given by τ_{ab} and its decay will be given by the loss of e_b population, τ_{bL} . The signal strength is weighted by the transition dipole magnitudes of the four laser interactions, in this case $|\mu_a|^2 |\mu_b|^2$.

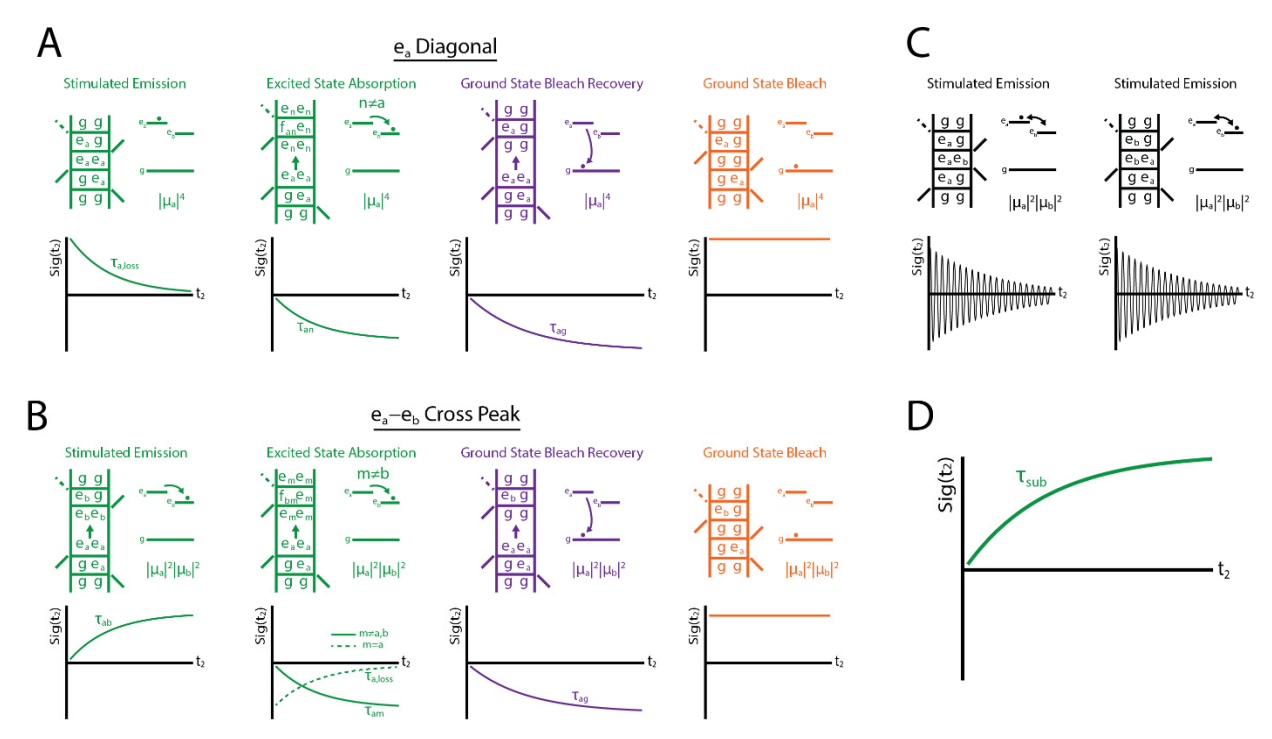


Figure 2. Excitonic Feynman pathways between diagonal peaks and corresponding below diagonal cross peaks possess dynamical symmetries that allow for isolation of population transfer signals. The major contributing pathways to these peaks (A, B) are stimulated emission, excited state absorption, ground state bleach recovery, and ground state bleach signals. The ground state bleach recovery signals evolve with the same kinetics given by τ_{ag} on both peaks, but the stimulated emission pathways evolve according to their respective population transfer kinetics. The τ_{ag} time is typically much larger than energy transfer time constants, though they are plotted here on a similar scale for clarity. One pair of excited state absorption pathways evolve with identical t₂ kinetics as the stimulated emission signals, while the others are subtracted out (see Figure S2). The four pathways on the diagonal and cross peak have the transition dipole strength $|\mu_a|^4$ for the diagonal and $|\mu_a|^2 |\mu_b|^2$ for the cross peak. The total signal of both the diagonal and cross peaks will decay to zero as the system reaches equilibrium because the SE and ESA pathways each decay as the excited state is depleted and because the GSB-R cancels the GSB signal. C) Coherence pathways do not contribute to the monotonic evolution of the total signal. D) The normalized diagonal and cross peak signals can be subtracted to remove the bleach recovery pathways and symmetrical excited state absorption pathways. What remains is a signal whose kinetics evolve according to population transfer. The subtracted signal can be used as a parameter to fit to energy transfer time constants. Note: for each rephasing pathway that undergoes population evolution during t_2 , there is a corresponding nonrephasing pathway that undergoes the same population time dynamics, not shown here for brevity.

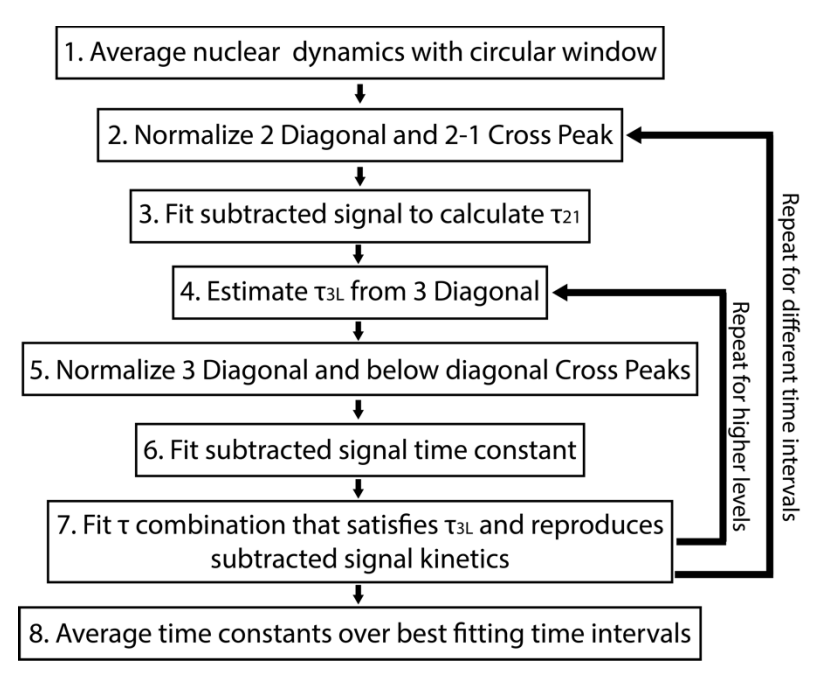


Figure 3. Scheme for extracting kinetic time constants from two-dimensional spectroscopic signals. Time constants are calculated from lowest to highest exciton energy. The entire procedure is repeated for multiple time intervals, and those with the best fitting subtracted time trace are averaged to generate the most accurate time constants.

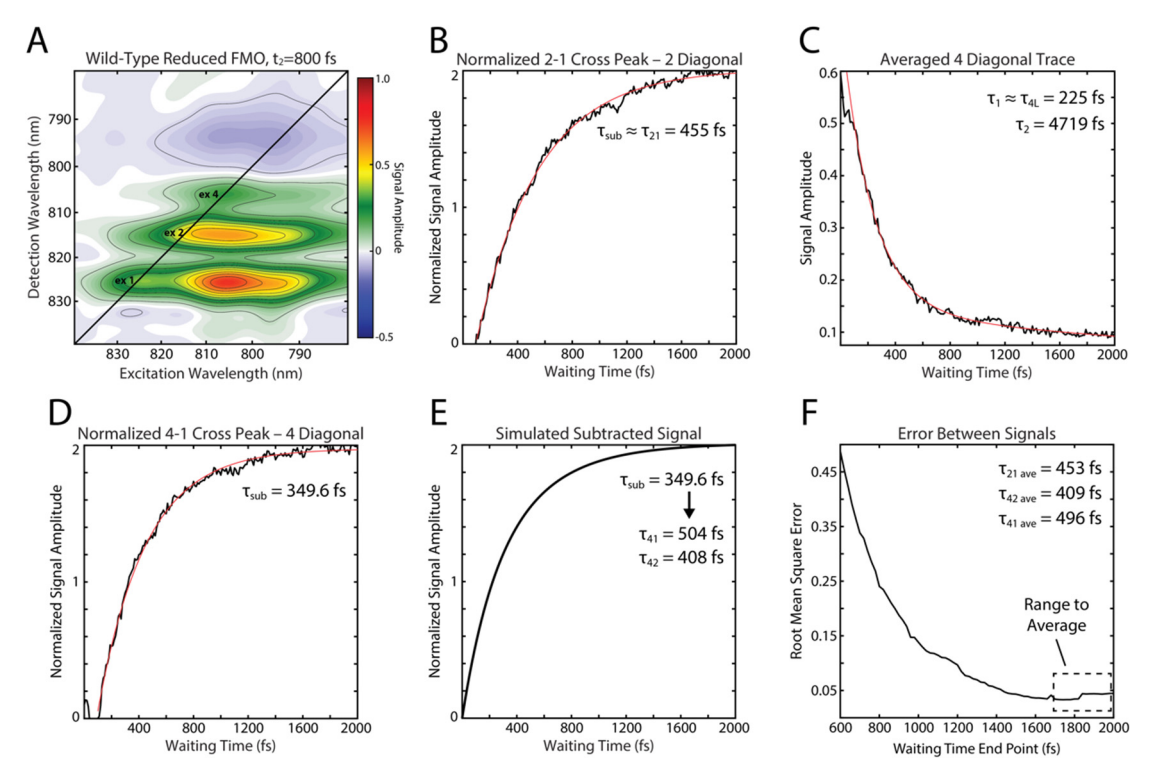


Figure 4. Demonstration of the analysis method using the Fenna-Matthews-Olson complex. A) Absorptive population time spectrum at t_2 =800 fs. Shown are the exciton 1, 2, and 4 diagonal peaks and their corresponding below diagonal cross peaks. Each peak region is averaged using a 70 cm⁻¹ window. B) Fit to the normalized 2 diagonal subtracted from the normalized 2-1 cross peak traces. The monoexponential time constant is approximately equal to the τ_{21} energy transfer time constant 455 fs. C) Biexponential fit to the averaged exciton 4 diagonal trace. The first time constant is used as the 4 loss time. D) Fit to the normalized 4 diagonal subtracted from the normalized 4-1 cross peak traces. E) Simulated subtracted signal reproduces the signal time constant in panel (D) using τ_{41} =504 fs and τ_{42} =408 fs, which satisfies the constraint of τ_{4L} . F) This process is repeated using a series of population time ranges, and the root-mean-square error between the signals in (D) and (E) are calculated. The time constants are averaged over the lowest error region to obtain the final energy transfer time constants.

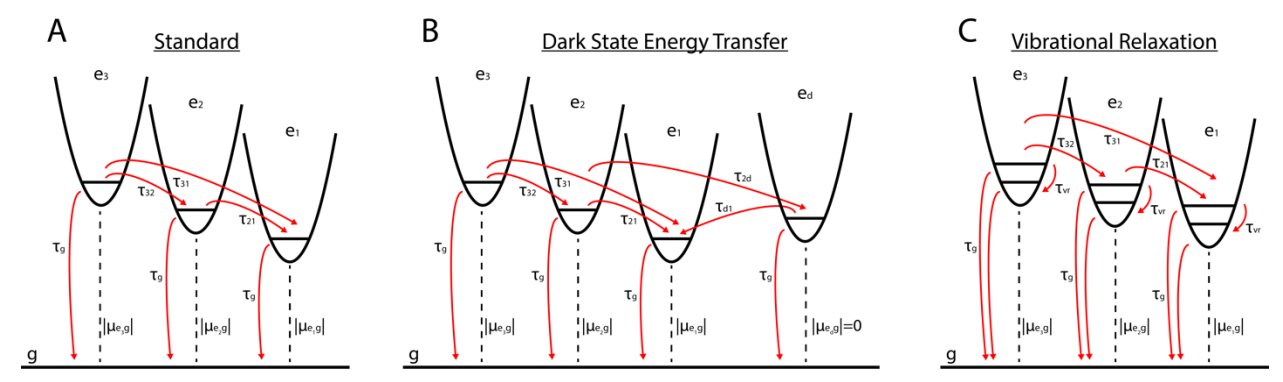


Figure 5. Three types of systems are used in global response calculations. A) Standard electronic system with three bright excitonic states allowing downhill energy transfer and slow relaxation to the ground state. B) Dark state system, where a fourth excitonic state is added to the standard system. This state has no oscillator strength with the ground state but still participates in downhill energy transfer with other excitons. Shown is a dark state between excitons 2 and 1, but the same analysis is also conducted using a dark state between excitons 3 and 2. C) Vibrational system, where vibrational modes resonant with the exciton energy gap are added to the standard system. Vibrational relaxation constructively interferes with below diagonal cross peak dynamics and slows the signal evolution.

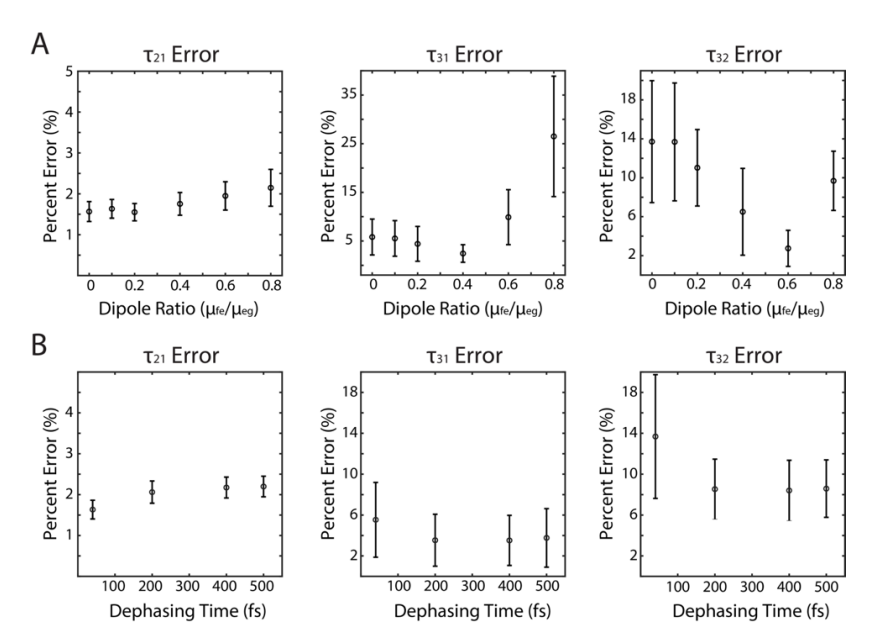


Figure 6. Error analysis for interfering excited state absorption and coherence pathways in the kinetic extraction method for a variety of time constants in the standard system. A) Percent error for each time constant as a function of relative transition dipole magnitude between μ_{fe} and μ_{eg} , which corresponds to the relative signal strength of the excited state absorption and ground state bleach/stimulated emission pathways, respectively. B) Percent error as a function of dephasing time for excited state electronic coherences. Long-lived coherences have little effect on the accuracy of the method because they do not contribute to monotonic signal growth or decay.

TOC Graphic

